Phase structure of electroweak vacuum in a strong magnetic field: the lattice results

M.N. Chernodub, V.A. Goy, A.V. Molochkov

Phase structure of electroweak vacuum in a strong magnetic field: the lattice results

M. N. Chernodub,[1] V. A. Goy,[2] and A. V. Molochkov[2]

[1] *Institut Denis Poisson UMR 7013, Université de Tours, 37200 Tours, France*
[2] *Pacific Quantum Center, Far Eastern Federal University, 690950 Vladivostok, Russia*

(Dated: December 13, 2022)

Using first-principle lattice simulations, we demonstrate that in the background of a strong magnetic field (around $10^{20}\,\mathrm{T}$), the electroweak sector of the vacuum experiences two consecutive crossover transitions associated with dramatic changes in the zero-temperature dynamics of the vector W bosons and the scalar Higgs particles, respectively. Above the first crossover, we observe the appearance of large, inhomogeneous structures consistent with a classical picture of the formation of W and Z condensates pierced by vortices. The presence of the W and Z condensates supports the emergence of the exotic superconducting and superfluid properties induced by a strong magnetic field in the vacuum. We find evidence that the vortices form a disordered solid or a liquid rather than a crystal. The second transition restores the electroweak symmetry. Such conditions can be realized in the near-horizon region of the magnetized black holes.

Powerful magnetic-field background can modify the physical properties of the vacuum. For electromagnetic interactions described by Quantum Electrodynamics, the relevant intensity of the magnetic field is set by the Schwinger limit, $B^{\mathrm{QED}} = m_e^2/e \simeq 4 \times 10^9\,\mathrm{T}$ [1] determined by the electron mass m_e [2]. At this strength – which is already bypassed by the fields near the surface of magnetars [3] – the vacuum acquires optical birefringence properties [4] and can act as a "magnetic lens" which can distort and magnify images [5] similarly to the celebrated galaxy-scale gravitational lengths.

Strong fundamental interactions, described by Quantum Chromodynamics, are affected by the magnetic field of the strength of the hadronic mass scale, $B^{\mathrm{QCD}} \sim m_p^2/e \sim 10^{16}\,\mathrm{T}$ where m_p is the proton mass. Such fields generate the magnetic catalysis [6–8], which implies, in particular, a persistent enhancement of the chiral symmetry breaking in the QCD vacuum as the external magnetic field strengthens. The QCD vacuum can also acquire electromagnetic superconducting properties supported by condensation of electrically charged mesonic bound states with vector, ρ-meson quantum numbers [9]. The transient magnetic fields of relevant scales appear in non-central and ultra-peripheral heavy-ion collisions at RHIC and LHC facilities [10, 11].

Electroweak fundamental interactions provide us with an additional source of vacuum instability at the critical magnetic field [12–14]:

$$B_{c1} \equiv B_{c1}^{\mathrm{EW}} = \frac{m_W^2}{e} \simeq 1.1 \times 10^{20}\,\mathrm{T}\,, \qquad (1)$$

determined by the mass $m_W \simeq 80.4\,\mathrm{GeV}$ of the W boson. It was suggested that this instability marks the onset of the condensation of the W bosons which can be inferred from the classical equations of motion of the electroweak model [13–18]. The condensate solution corresponds to a crystalline order of parallel vortex-like structures that shares geometric similarity with the lattice of Abrikosov vortices of a conventional type-II superconductor: for realistically heavy Higgs masses, $m_H > m_Z$, the vortices in the W condensate arrange themselves into a hexagonal lattice [15, 19, 20]. This exotic vacuum state should possess unusual anisotropic superconducting [9] and superfluid [21] properties [22]. The W condensation may also develop in the cores of electroweak strings [23–26].

The electroweak vacuum is suggested to experience the second transition at an even higher magnetic field:

$$B_{c2} \equiv B_{c2}^{\mathrm{EW}} = \frac{m_H^2}{e} \simeq 2.7 \times 10^{20}\,\mathrm{T}\,, \qquad (2)$$

determined by the Higgs mass $m_H = 125.1\,\mathrm{GeV}$. Above B_{c2}, the electroweak symmetry should be restored [18, 27, 28]. In this phase, the vortex lattice evaporates leaving some traces in this new phase [29, 30]. The magnetic fields of the relevant $10^{20}\,\mathrm{T}$ scale might have been created at the cosmological electroweak phase transition in the first moments of the Early Universe [31, 32]. Such enormous fields were suggested to exist even in the modern Universe in the vicinity of the magnetized black holes [33, 34].

Our work aims to establish, using the first-principle lattice simulations, the phase structure of the vacuum subjected to magnetic fields of the electroweak strength. Despite the "weak" name, such fields are among the most powerful magnetic fields that were rarely discussed in the context of the Standard Model of particles.

The discussions of the effect of magnetic fields on the vacuum structure reveal certain controversies in the literature. The transition to the inhomogeneous superconducting phase of the electroweak (EW) vacuum proceeds via the instability of the vacuum at the first critical field (1) because at $B > B_{c1}$, the ground state W mass becomes a purely imaginary quantity, $m_W^2(B) = m_W^2 - |eB|$. At the classical level, the formation of the periodic vortex lattice in the background magnetic field has been established in the EW model [35]. However, this classical-level scenario, together with the arguments based on loop computations [12] has been questioned in

Ref. [36] where it was shown that quantum corrections could add a radiative term to the classical W mass in such a way that the mass does not vanish at the critical field $B = B_{c1}$. Consequently, it was concluded that no thermodynamic instability should occur in the Electroweak sector. Earlier numerical simulations of the electroweak model in the background magnetic field did not reveal the presence of the vortex-dominated phase around the finite-temperature electroweak crossover [37] which could be explained by a destructive role of thermal fluctuations.

A similar no-go theorem was suggested to forbid the superconducting transition in QCD vacuum [38]. The instability in QCD should proceed via the spontaneous ρ-meson condensation similarly to the magnetic-field induced condensation of the W bosons in the EW model [9]. The fact that the ρ-meson mass does not vanish at any magnetic field was later supported by the effective model calculations [39] as well as the first-principle numerical simulations [40]. However, despite the absence of the thermodynamic singularity at finite magnetic field B, it was argued that the large-B superconducting phase can still emerge via a smooth crossover transition implying that the transition to the new phase occurs at nonvanishing ρ-meson mass in the absence of a thermodynamic singularity [41]. The latter scenario has a speculative nature that requires confirmation from a first-principle simulation. To this end, the electroweak model provides us with an exciting playground, given the similarity of the superconducting mechanisms in both systems.

We consider the bosonic sector of the Electroweak model with the Lagrangian

$$\begin{aligned}\mathcal{L}_{\rm EW} = &-\frac{1}{2}{\rm Tr}\,(W_{\mu\nu}W^{\mu\nu}) - \frac{1}{4}Y_{\mu\nu}Y^{\mu\nu} \\ &+(D_\mu\phi)^\dagger(D^\mu\phi) - V(\phi),\end{aligned} \tag{3}$$

where the field strengths of, respectively, the SU(2) gauge field W^a_μ and $U(1)_Y$ hypercharge gauge field Y_μ are

$$W^a_{\mu\nu} = \partial_\mu W^a_\nu - \partial_\nu W^a_\mu + ig\varepsilon^{abc}W^b_\mu W^c_\nu\,, \tag{4}$$

$$Y_{\mu\nu} = \partial_\mu Y_\nu - \partial_\nu Y_\mu\,, \tag{5}$$

These vector fields interact with the complex scalar Higgs doublet $\phi \equiv (\phi_1, \phi_2)^T$ via the covariant derivative:

$$D_\mu = \partial_\mu + \frac{i}{2}gW^a_\mu\sigma^a + \frac{i}{2}g'Y_\mu, \tag{6}$$

where σ^a ($a = 1, 2, 3$) are the Pauli matrices. The ratio of the $U(1)$ and $SU(2)$ gauge couplings, $g'/g = \tan\theta_W$, defines the electroweak mixing (Weinberg) angle θ_W fixed in experiments [42]: $\sin^2\theta_W \equiv 1 - m^2_W/m^2_Z = 0.22290(30)$.

The last term in the Lagrangian (3) is the potential $V(\phi) = \lambda\left(\phi^\dagger\phi - v^2/2\right)^2$ of the Higgs field doublet ϕ, where λ is the dimensionless self-coupling of the Higgs field and the only dimensionful parameter v sets the vacuum expectation value of the Higgs field.

In the broken phase, the Higgs field acquires the mass $m_H = \sqrt{2\lambda}v$. The theory possesses the massless photon,

$$A_\mu = W^3_\mu\sin\theta_W + Y_\mu\cos\theta_W\,, \tag{7}$$

and three massive gauge bosons which include the electrically (off-diagonal) charged W bosons $W^\pm_\mu = W^1_\mu \pm iW^2_\mu$, and the neutral (diagonal) Z boson:

$$Z_\mu = W^3_\mu\cos\theta_W - Y_\mu\sin\theta_W\,, \tag{8}$$

with the masses $m_W = gv/2$ and $m_Z = m_W/\cos\theta_W$.

We consider the electroweak vacuum in the background of the hypermagnetic field $\boldsymbol{B}_Y = \boldsymbol{\nabla}\times\boldsymbol{Y}$ corresponding to the hypergauge field $Y^\mu = (Y^0, \boldsymbol{Y})$. In the broken phase, the two fields are related to each other:

$$g'\boldsymbol{B}_Y = e\boldsymbol{B} \qquad [\text{broken phase}]\,, \tag{9}$$

as it follows from the definition of the elementary electric charge, $e = g\sin\theta_W = g'\cos\theta_W = gg'/\sqrt{g^2+g'^2}$, Eqs. (7) and (8), as well as from the fact that in the broken phase, the Z boson is a massive particle which carries no global flux. In the symmetry-restored phase, where the magnetic field $\boldsymbol{B}$ cannot be defined, the hypermagnetic field $\boldsymbol{B}_Y$ plays a role of a genuine field.

Using the first-principle Monte Carlo techniques, we simulate the lattice version of the EW model (3). The standard lattice discretization of the model, the known particularities of the lattice (hyper)magnetic field, the technicalities related to the choice of lattice parameters, and the lattice form of the physical observables discussed in the paper are described in the Supplemental Material, Sections A, B, C, and D respectively.

In Fig. 1(a) we show the (normalized) vacuum expectation value of the absolute value of the Higgs field squared $\langle|\phi|^2\rangle$ as the function of the background (hyper)magnetic field $g'B_Y$. In agreement with the theoretical analysis, one observes three regions (phases) separated by two inflection points of the Higgs condensate. We found the following values of the pseudocritical magnetic field:

$$g'B_{Y,c1} \equiv eB_{c1} = 0.68(5)m^2_W\,, \tag{10}$$

$$g'B_{Y,c2} \equiv eB_{c2} = 0.99(2)m^2_H\,. \tag{11}$$

The first critical field (10) turns out to be about 30% weaker than the value (1) predicted by the classical theoretical analysis that does not take into account quantum fluctuations. However, the second critical field (11) agrees precisely with the theoretical value (2).

The classical picture predicts that the magnetic field affects the Higgs condensate as follows [12–19, 27, 28]:

(i) In the broken phase ($B < B_{c1}$), the Higgs condensate does not depend on the magnetic field B.

(ii) When B exceeds the first critical value $B = B_{c1}$, the vacuum develops a raising W condensate which gradually inhibits the Higgs condensate.

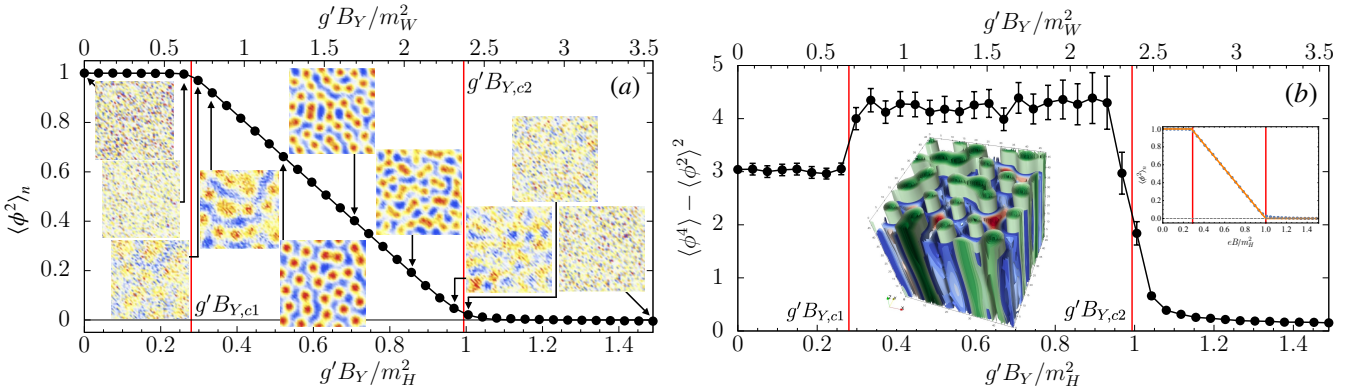

FIG. 1. (a) Normalized value $\langle\phi^2\rangle_n = \phi_r^2(B_Y)/\phi_r^2(0)$ of the additively renormalized, volume-averaged, $\phi^2 \equiv \frac{1}{V}\int \phi^\dagger\phi$, (squared) Higgs condensate $\phi_r^2(B_Y) = \langle\phi^2(B_Y)\rangle - \langle\phi^2(\infty)\rangle$. The insets show the density plots of the Z_{12} fluxes in the cross-sections normal to the magnetic field axis in typical configurations (more details are provided in the description of Fig. 3). (b) The susceptibility of the Higgs field squared vs. the hypermagnetic field B_Y. The right inset shows the fit of the Higgs condensate shown in (a) by the piecewise function (12). The left inset illustrates a typical 3d configuration in the inhomogeneous phase in the (hyper)magnetic field background $g'B_Y = eB = 1.1m_W^2$ (the total number of vortices is 24). The equipotential surfaces of the W condensate (the Higgs condensate) are shown in blue and red (green). These quantities, which take their maximal values at the centers of the corresponding structures, are shown in complimentary regions. We used a cooling procedure to improve visibility of this 3d picture. The vertical red lines denote the transitions.

(iii) Finally, as the field reaches the second critical value, $B = B_{c2}$, the Higgs condensate should vanish, and the electroweak theory should be restored.

All these properties are spectacularly confirmed by our numerical simulations shown in Fig. 1(a) [43].

The observed dependence of the Higgs expectation value on magnetic field, shown in Fig. 1(b), can be described by an impressively simple piecewise-linear formula predicted by the theory [18, 21, 44, 45]:

$$\frac{\langle\phi^2\rangle_r(B)}{\langle\phi^2\rangle_r(0)} = \begin{cases} 1, & B < B_{c1}, \\ \frac{B_{c2}-B}{B_{c2}-B_{c1}}, & B_{c1} < B < B_{c2}, \\ 0, & B > B_{c2}, \end{cases} \qquad (12)$$

which fits our data everywhere except for small regions around the (pseudo)critical points $B = B_{c1}$ and $B = B_{c2}$.

The structure of the classical solution around B_{c1} implies that the first phase transition should be of the second order [17, 21]. In this case, the susceptibility of the Higgs field should possess a local maximum at the (pseudo)critical point. We do not see any peaks in the susceptibility across neither B_{c1} nor B_{c2}, Fig. 1(b). Thus, these transitions are smooth crossovers.

The W condensates are shown in Fig. 2. In an excellent qualitative agreement with the theory (the right inset), the squared $W_\perp^2$ condensate raises linearly in the intermediate phase. The observed slope of the linear part, $\partial|W_\perp|^2/\partial(eB) \simeq 2.9$, is about 30% larger than the slope predicted by the classical solution, $\partial|W_\perp|^2/\partial(eB) \simeq 2.1$ [21]. This deviation indicates the important role of the quantum fluctuations responsible also for the 30% shift of the first critical field B_{c1}. In the restored phase at $B > B_{c2}$, the W condensate flattens, possibly indicating the presence of the condensate of "zero-field twists"

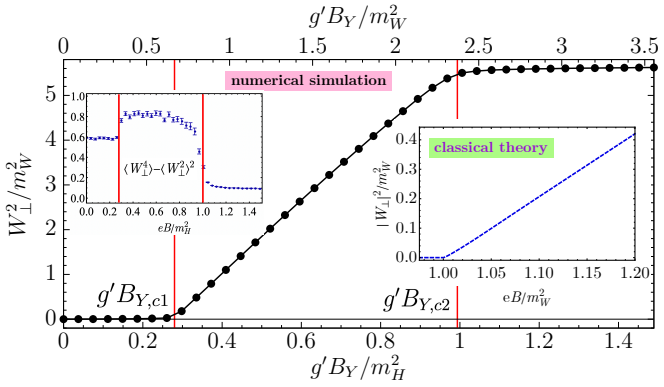

FIG. 2. The numerical result for the expectation value of the W condensate vs. the (hyper)magnetic field $g'B_Y = eB$. The right inset is the theoretical result based on the classical solution for the transverse W condensate squared [21]. The left inset shows the susceptibility of the transverse W condensate.

which are suggested to be the remnants of the vortex lattice [29] visible close to $B = B_{c2}$ [30]. The W susceptibility (the left inset) exhibits close similarity with the susceptibility of the Higgs field shown in Fig. 1(b).

To confront our theoretical expectation with the first principle simulations, we visualize in Fig. 3 the structure of the electroweak fields in the cross-section perpendicular to the magnetic field axis (we take $\boldsymbol{B}$ in the z direction). We show analytical results in the classical theory in Figs. 3(a)-(d) and visualize the numerical data obtained in lattice simulations in Figs. 3(e)-(m). The numerical results were obtained by taking an average over a few dozen successive field configurations generated in the background of the (hyper)magnetic field

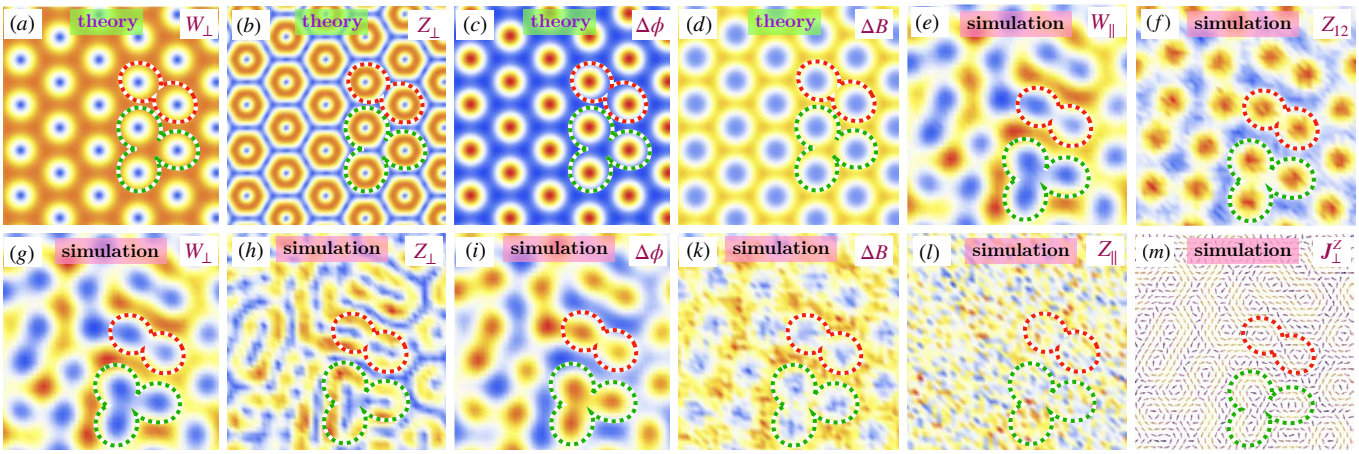

FIG. 3. Density plots of various quantities in the cross-sections normal to the axis of the (hyper)magnetic field. Theoretical results, (a)-(d), are given for the classical solution of Ref. [21] at $B = 1.01B_c$. The numerical results of the first-principle simulations, (e)-(m), are given for a typical lattice configuration in the background of the (hyper)magnetic field $g'B_Y \equiv eB \simeq 1.1m_W^2 \simeq 1.6eB_{c1}$ (the magnetic number $k = 12$ for our lattices). (a) and (g): transverse W condensate $W_\perp = \sqrt{|W_x|^2 + |W_y|^2}$; (b) and (h): transverse Z condensate $Z_\perp = \sqrt{|Z_x|^2 + |Z_y|^2}$; (c) and (i) local excess of the Higgs expectation value over the condensate, $\Delta\phi(\boldsymbol{x}) = \phi(\boldsymbol{x}) - \langle\phi\rangle$; (d) and (k): local excess of the magnetic field value over the background, $\Delta B(\boldsymbol{x}) = B(\boldsymbol{x}) - B_{\rm ext}$; (e) and (l): longitudinal W and Z condensates, $W_\parallel = |W_z|$ and $Z_\parallel = |Z_z|$, respectively (theoretically, $W_\parallel = Z_\parallel = 0$ at the classical level); (f): the Z-flux; (m) the neutral Higgs currents $\boldsymbol{J}^Z_\perp$. The red (blue) colors correspond to maxima (minima); absolute values are given for complex quantities. The same regions are circumvented by the red and green dashed lines (separately for the analytical solution and simulated configuration) to guide the eye. More details are given in the text.

$g'B_Y \equiv eB \simeq 1.1m_W^2$ which corresponds to the intermediate phase in between two critical fields $B_{c1} < B < B_{c2}$.

According to the theoretical expectations [15, 18, 19], the ground state of the intermediate phase corresponds to a spatially inhomogeneous structure made of the W condensate with nonvanishing transverse components W_x and W_y. The inhomogeneities are produced by vortices that are embedded in the condensate. The vortices should arrange themselves into a hexagonal pattern in the plane perpendicular to the magnetic field. The transverse component of the W condensate, $W_\perp = \sqrt{|W_x|^2 + |W_y|^2}$, should vanish in the core of each vortex, Fig. 3(a).

Instead of the hexagonal pattern of the classical solution, Fig. 3(a), our lattice simulations reveal a less regular structure, Fig. 3(g). However, similarly to the classical solution, the lattice field $W_\perp$ exhibits a semi-classical behavior characterized by large, both in magnitude and in size structures [46]. We associate these structures with the inhomogeneous W condensate. The condensate exhibits a set of separate deep minima which point to the presence of the vortex cores in agreement with the theoretical classical picture, Fig. 3(a). Modulo occasional overlaps, the total number of vortices at chosen magnetic number $k = 12$ appears to be equal to 24, which corresponds to the number $2k$ of the elementary fluxes of hypermagnetic field, as expected.

Contrary to the expectations based on the classical theory, Fig. 3(a), the vortices do not form the crystalline phase in the vacuum, Fig. 3(g). While some traces of the crystalline vortex order are seen, the quantum fluctuations disorder the classical hexagonal structure so that the vortices form a disordered solid or, possibly, a liquid. The formation of the vortex liquid phase is not unexpected, though, as it has been proposed, in a similar non-Abelian context, in Ref. [47].

According to the classical picture, the transverse Z condensate $Z_\perp = \sqrt{|Z_x|^2 + |Z_y|^2}$ forms a regular honeycomb structure, Fig. 3(b). This neutral condensate vanishes in the center of each vortex and a honeycomb-like manifold in between the vortices. The regions with nonzero Z condensate are thin pipe-like shells surrounding the vortex cores. Strikingly, these classical structures, disordered by quantum fluctuations, are also seen in our lattice configurations, Fig. 3(h): the thin shells of the Z condensate surround the cores of vortices.

The classical EW theory predicts that in the cores of vortices, the Higgs condensate should get enhanced [21], Fig. 3(c), while the magnetic field should be locally suppressed due to the anti-screening effect [14], Fig. 3(d). These properties, which defy our intuition based on the Abrikosov picture of type-II superconductors, are confirmed by the results of our numerical simulations shown in Figs. 3(i) and (k), respectively. A 3d picture of the Higgs and W condensates and the magnetic field lines of a typical configuration is shown in the inset of Fig. 1(b).

We also noticed that $|W_x| \simeq |W_y|$ holds high precision in numerical simulations. The unexpected outcome of our simulations is the presence of the large longitudinal condensate $W_\parallel \simeq W_\perp$, Fig. 3(e) which closely mimics the transverse condensate, Fig. 3(g). This observation

disagrees with the classical theory that predicts $W_{\parallel} = 0$ in the ground state. On the contrary, the condensate of the z component of the neutral Z boson is vanishing in agreement with the classical picture: we observe only small quantum fluctuations in this quantity, Fig. 3(l).

Numerically, the Z_{12} flux provides us with the most transparent view of the vortex content of field configurations, Fig. 3(f). The peaks in the Z flux point out to the positions of the vortex cores also seen as the deeps in the W condensate, Fig. 3(e), the spikes in the Higgs condensate, Fig. 3(g), and, much less clear, as the minima in the magnetic field, Fig. 3(h). The associated neutral currents $\boldsymbol{J}^Z$ of the Higgs field, Fig. 3(m), defined as a variation of the matter part of the action with respect to the Z field, circumvents the vortices.

In the inset of Fig. 1(a), we show the evolution of the Z flux density in the transverse plane of the gradually increasing (hyper)magnetic field. The vortices start to form as soon as the magnetic field crosses the first pseudocritical value, $B = B_{c1}$. The vortex structures are barely seen. The fuzziness of vortex positions appears due to the weakness of the condensates right above the critical point. This property makes the weak classical structure vulnerable to the disorder caused by ultraviolet fluctuations and phonons in the vortex lattice that lead to the drifting of the vortex cores. The vortices may form a liquid close to the first critical field B_{c1}.

In the middle of the superconducting phase, the vortex liquid partially solidifies into a disordered solid. The physical motion of the vortices leads to enhanced local fluctuations of all physical quantities that experience extrema at or around vortex cores. In particular, the vortex motion enhances fluctuations of the Higgs condensate, thus leading to the elevated values of the Higgs and W susceptibilities in the inhomogeneous phase that we already observed in Fig. 1(b) and Fig. 2, respectively.

Close to the second critical field, $B = B_{c2}$, the vortex solid starts to melt. Finally, the vortices disappear entirely as the vacuum crosses into the third phase at $B > B_{c2}$, where the electroweak symmetry gets restored.

In support of earlier theoretical suggestions [9, 21], the presence of classically significant W and Z condensates points to the fascinating possibility that in the strong magnetic field, the vacuum becomes an electromagnetic superconductor enriched by a neutral superfluid component that support dissipationless transport along magnetic field lines. In the present time, such conditions can be realized in the vicinity of the magnetized black holes [33, 34].

Acknowledgments. M.C. is grateful to M. Shaposhnikov for illuminating discussions. The numerical simulations were performed at the Supercomputer SQUID (Osaka University, Japan) and the computing cluster Vostok-1 of Far Eastern Federal University. V.G. has been supported by RSF (Project No. 21-72-00121) (code development, simulation, data analysis). A.M. has been partially supported within the state assignment of the Ministry of Science and Higher Education of Russia (Project No. 0657-2020-0015) (theoretical interpretation). M.C. has been partially supported by the project IEA-International Emerging Actions No. 00677 (wrote the text, theoretical interpretation, structure of paper).

[1] We use the units $\hbar = c = 1$.
[2] J. S. Schwinger, Phys. Rev. **82**, 664 (1951).
[3] S. Olausen and V. Kaspi, The Astrophysical Journal Supplement Series **212**, 6 (2014).
[4] S. L. Adler, Annals Phys. **67**, 599 (1971).
[5] N. J. Shaviv, J. S. Heyl, and Y. Lithwick, Monthly Notices of the Royal Astronomical Society **306**, 333 (1999).
[6] S. P. Klevansky and R. H. Lemmer, Phys. Rev. D **39**, 3478 (1989).
[7] K. G. Klimenko, Z. Phys. C **54**, 323 (1992).
[8] I. A. Shovkovy, Lect. Notes Phys. **871**, 13 (2013), arXiv:1207.5081 [hep-ph].
[9] M. N. Chernodub, Phys. Rev. D **82**, 085011 (2010), arXiv:1008.1055 [hep-ph].
[10] V. Skokov, A. Y. Illarionov, and V. Toneev, Int. J. Mod. Phys. A **24**, 5925 (2009), arXiv:0907.1396 [nucl-th].
[11] W.-T. Deng and X.-G. Huang, Phys. Rev. C **85**, 044907 (2012), arXiv:1201.5108 [nucl-th].
[12] N. K. Nielsen and P. Olesen, Nucl. Phys. B **144**, 376 (1978).
[13] V. Skalozub, Sov. J. Nucl. Phys.(Engl. Transl.);(United States) **28** (1978).
[14] J. Ambjorn and P. Olesen, Phys. Lett. B **214**, 565 (1988).
[15] V. V. Skalozub, Sov. J. Nucl. Phys. **45**, 1058 (1987).
[16] J. Ambjorn and P. Olesen, Nucl. Phys. B **315**, 606 (1989).
[17] J. Ambjorn and P. Olesen, Phys. Lett. B **218**, 67 (1989), [Erratum: Phys.Lett.B 220, 659 (1989)].
[18] J. Ambjorn and P. Olesen, Nucl. Phys. B **330**, 193 (1990).
[19] S. W. MacDowell and O. Tornkvist, Phys. Rev. D **45**, 3833 (1992).
[20] O. Tornkvist, (1992), arXiv:hep-ph/9204235.
[21] M. N. Chernodub, J. Van Doorsselaere, and H. Verschelde, Phys. Rev. D **88**, 065006 (2013), arXiv:1203.5963 [hep-ph].
[22] The vacuum superconductivity at QCD [9] and Electroweak [9, 21] scales is similar to reentrant superconductivity which is suggested to occur in clean superconducting materials in very high magnetic fields [48].
[23] A. Achucarro, R. Gregory, J. A. Harvey, and K. Kuijken, Phys. Rev. Lett. **72**, 3646 (1994), arXiv:hep-th/9312034.
[24] W. B. Perkins, Phys. Rev. D **47**, R5224 (1993).
[25] P. Olesen, (1993), arXiv:hep-ph/9310275.
[26] J. Garaud and M. S. Volkov, Nucl. Phys. B **826**, 174 (2010), arXiv:0906.2996 [hep-th].
[27] A. Salam and J. A. Strathdee, Nucl. Phys. B **90**, 203 (1975).
[28] A. D. Linde, Phys. Lett. B **62**, 435 (1976).
[29] P. Olesen, Phys. Lett. B **268**, 389 (1991).
[30] J. Van Doorsselaere, Phys. Rev. D **88**, 025013 (2013), arXiv:1206.6205 [hep-ph].
[31] T. Vachaspati, Phys. Lett. B **265**, 258 (1991).
[32] D. Grasso and H. R. Rubinstein, Phys. Rept. **348**, 163 (2001), arXiv:astro-ph/0009061.

[33] J. Maldacena, JHEP **04**, 079 (2021), arXiv:2004.06084 [hep-th].

[34] D. Ghosh, A. Thalapillil, and F. Ullah, Phys. Rev. D **103**, 023006 (2021), arXiv:2009.03363 [hep-ph].

[35] D. L. J. Ho and A. Rajantie, Phys. Rev. D **102**, 053002 (2020), arXiv:2005.03125 [hep-th].

[36] V. V. Skalozub, Phys. Atom. Nucl. **77**, 901 (2014).

[37] K. Kajantie, M. Laine, J. Peisa, K. Rummukainen, and M. E. Shaposhnikov, Nucl. Phys. B **544**, 357 (1999).

[38] Y. Hidaka and A. Yamamoto, Phys. Rev. D **87**, 094502 (2013), arXiv:1209.0007 [hep-ph].

[39] M. A. Andreichikov, B. O. Kerbikov, V. D. Orlovsky, and Y. A. Simonov, Phys. Rev. D **87**, 094029 (2013), arXiv:1304.2533 [hep-ph].

[40] G. S. Bali, B. B. Brandt, G. Endrődi, and B. Gläßle, Phys. Rev. D **97**, 034505 (2018).

[41] M. N. Chernodub, Phys. Rev. D **89**, 018501 (2014), arXiv:1309.4071 [hep-ph].

[42] E. Tiesinga, P. J. Mohr, D. B. Newell, and B. N. Taylor, Journal of Physical and Chemical Reference Data **50**, 033105 (2021).

[43] The vanishing of the condensate at $B > B_{c2}$ is not evident without an additional analysis since the quantity $\langle \phi^2 \rangle$ is affected by significant ultraviolet contributions both in broken and unbroken phases. However, the homogenisation of the W condensate above B_{c2} indicates that the vanishing Higgs condensate disorders the magnetic field over the entire electroweak group.

[44] J. Ambjorn and P. Olesen, Int. J. Mod. Phys. A **5**, 4525 (1990).

[45] J. Ambjorn and P. Olesen, in *4th Hellenic School on Elementary Particle Physics* (1992) pp. 396–406, arXiv:hep-ph/9304220.

[46] We do not perform any smoothening or cooling procedures that could drive our Monte Carlo configurations of Figs. 3(e)-(m) closer to the classical regime.

[47] J. Ambjorn and P. Olesen, Nucl. Phys. B **170**, 60 (1980).

[48] M. Rasolt and Z. Tešanović, Rev. Mod. Phys. **64**, 709 (1992).

[49] W. Langguth, I. Montvay, and P. Weisz, Nucl. Phys. B **277**, 11 (1986).

[50] B. Bunk, E.-M. Ilgenfritz, J. Kripfganz, and A. Schiller, Phys. Lett. B **284**, 371 (1992).

[51] B. Bunk, E.-M. Ilgenfritz, J. Kripfganz, and A. Schiller, Nucl. Phys. B **403**, 453 (1993).

[52] Z. Fodor, J. Hein, K. Jansen, A. Jaster, and I. Montvay, Nucl. Phys. B **439**, 147 (1995), arXiv:hep-lat/9409017.

[53] Z. Fodor, J. Hein, K. Jansen, A. Jaster, I. Montvay, and F. Csikor, Phys. Lett. B **334**, 405 (1994), arXiv:hep-lat/9405021.

[54] F. Csikor, Z. Fodor, J. Hein, A. Jaster, and I. Montvay, Nucl. Phys. B **474**, 421 (1996), arXiv:hep-lat/9601016.

[55] Y. Aoki, F. Csikor, Z. Fodor, and A. Ukawa, Phys. Rev. D **60**, 013001 (1999), arXiv:hep-lat/9901021.

[56] A. D. Sakharov, Pisma Zh. Eksp. Teor. Fiz. **5**, 32 (1967).

[57] V. A. Rubakov and M. E. Shaposhnikov, Usp. Fiz. Nauk **166**, 493 (1996), arXiv:hep-ph/9603208.

[58] K. Kajantie, K. Rummukainen, and M. E. Shaposhnikov, Nucl. Phys. B **407**, 356 (1993), arXiv:hep-ph/9305345.

[59] E.-M. Ilgenfritz, J. Kripfganz, H. Perlt, and A. Schiller, Phys. Lett. B **356**, 561 (1995), arXiv:hep-lat/9506023.

[60] M. Gurtler, E.-M. Ilgenfritz, J. Kripfganz, H. Perlt, and A. Schiller, Nucl. Phys. B **483**, 383 (1997), arXiv:hep-lat/9605042.

[61] K. Kajantie, M. Laine, K. Rummukainen, and M. E. Shaposhnikov, Nucl. Phys. B **493**, 413 (1997), arXiv:hep-lat/9612006.

[62] K. Kajantie, M. Laine, K. Rummukainen, and M. E. Shaposhnikov, Phys. Rev. Lett. **77**, 2887 (1996), arXiv:hep-ph/9605288.

[63] M. D'Onofrio and K. Rummukainen, Phys. Rev. D **93**, 025003 (2016), arXiv:1508.07161 [hep-ph].

[64] An equivalent, widely used formulation of the Higgs field in terms of an SU(2) matrix [49] gives identical results.

[65] G. S. Bali, F. Bruckmann, G. Endrodi, Z. Fodor, S. D. Katz, S. Krieg, A. Schafer, and K. K. Szabo, JHEP **02**, 044 (2012), arXiv:1111.4956 [hep-lat].

[66] C. Gattringer and C. B. Lang, *Quantum chromodynamics on the lattice*, Vol. 788 (Springer, Berlin, 2010).

[67] S. Durr, Comput. Phys. Commun. **172**, 163 (2005).

[68] R. Workman *et al.* (Particle Data Group), Prog. Theor. Exp. Phys. **083C01** (2022).

SUPPLEMENTAL MATERIAL

Section A: Lattice Electroweak model in hypermagnetic field background.

Most lattice simulations [50–55] of the electroweak model were performed at Higgs masses different from the physical value of the Higgs mass as these simulations were carried out before the Higgs particle was discovered experimentally. Moreover, since the main aim of the most simulations was to find the location and the strength of the electroweak transition (the latter property is essential for baryogenesis [56, 57]), a large number of simulations were done in a dimensionally reduced 3d lattice model valid at high temperatures [37, 58–62]. In addition, the hypercharge field Y_μ has been taken into account only in some studies [61, 63] because, in the absence of a background (hyper)magnetic field, the hypercharge sector plays a relatively modest role given the weakness of the hypercharge coupling g' and the Abelian nature of this field. Since our aim is different from most of the previous works, we simulate the model (i) with the physical Higgs mass (ii) in the four-dimensional formulation (iii) with the hypergauge field included. All these factors are required to uncover the properties of the electroweak vacuum in the background magnetic field.

We use the following lattice action for the theory (3):

$$\begin{aligned} S = {} & \beta \sum_{x,\mu<\nu} \left(1 - \frac{1}{2}\mathrm{Tr}\, U_{x,\mu\nu}\right) + \frac{\beta_Y}{2} \sum_{x,\mu<\nu} \theta^2_{x,\mu\nu} \\ & + \sum_x \left(-\kappa \phi^\dagger_x \phi_x + \lambda \left(\phi^\dagger_x \phi_x\right)^2\right) \\ & + \sum_{x,\mu} \left|\phi_x - e^{i\left(\theta_{x,\mu} + \theta^Y_{x,\mu}\right)} U_{x,\mu} \phi_{x+\hat{\mu}}\right|^2 , \end{aligned} \tag{13}$$

where ϕ_x is the Higgs doublet of two complex scalar fields [64].

In the leading order of a small lattice spacing a, the lattice SU(2) gauge field $U_{x,\mu}$ and the noncompact $U(1)$ hypercharge gauge field $\theta_{x,\mu}$ are related to their continuum counterparts A^a_μ and Y_μ, respectively, as follows: $U_{x,\mu} = e^{iat^a A^a_\mu(x)}$ and $\theta_{x,\mu} = aY_\mu(x)/2$, where $t^a = \sigma^a/2$ are the generators of the SU(2) gauge group expressed via the Pauli matrices σ^a. The lattice plaquettes $U_{x,\mu\nu} = U_{x,\mu} U_{x+\hat{\mu},\nu} U^\dagger_{x+\hat{\nu},\mu} U^\dagger_{x,\nu}$ and $\theta_{x,\mu\nu} = \theta_{x,\mu} + \theta_{x+\hat{\mu},\nu} - \theta_{x+\hat{\nu},\mu} - \theta_{x,\nu}$ correspond to the field strengths (4) and (5), respectively. Using a set of identifications, $\beta \to 4/g^2$ and $\beta_Y \to 4/g'^2$, as well as the rescalings $A_\mu \to gA_\mu$ and $Y_\mu \to g'Y_\mu$, we recover the continuum theory (3) from the lattice action (13).

The spatially uniform hypermagnetic field,

$$\boldsymbol{B}_Y = (0, 0, B_Y)\,, \qquad B_Y = \frac{2}{g'} \cdot \frac{2\pi k}{(L_s a)^2}\,, \tag{14}$$

is expressed in a standard way. The integer $k \in \mathbb{Z}$ determines the total number $2k$ of the elementary fluxes $\Phi_Y = 2\pi/g'$ carried by the hypermagnetic field through a lattice cross-section. In the lattice action (13), the hypermagnetic field (14) is introduced via the shift of the lattice hypercharge field $\theta_{\mathrm{x},\mu} \to \theta_{\mathrm{x},\mu} + \theta^Y_{\mathrm{x},\mu}$ similarly to the standard practices [65]. The flux quantization (14) appears as a result of periodic boundary conditions imposed in our calculations (more details are given in Appendix B).

In addition to the external hypergauge field $\theta^Y_{x,\mu}$, we have four parameters of the theory: β, β_Y, κ and λ. These parameters can be fixed via the requirement that the lattice model matches the known phenomenological parameters of the electroweak model at a zero magnetic field. As a matching criterion, we choose the mass ratios, m_W/m_H and m_Z/m_H (that also determine the Weinberg angle θ_W), and one of the charges, g or g' (the other one is determined by the Weinberg angle θ_W). A remaining degree of freedom corresponds to the variation in the lattice spacing a, which plays a role of an ultraviolet cutoff. The technical details highlighting our choice of lattice couplings are described in Appendix C.

We employ the Hybrid Monte Carlo technique to generate lattice field configurations [66]. For a zero value of the hypermagnetic field B_Y, we use about 16×10^6 configurations in order to fix the physical scale. For each nonzero value of B_Y, we work with about 10^6 configurations. We perform our calculations in the Euclidean lattice volume $L_t \times L_s^3$ with $L_t = 64$ and $L_s = 48$ corresponding to the zero-temperature limit.

Section B: Hypermagnetic field

This article aims to study the behavior of the electroweak model (3) in the background magnetic field $\boldsymbol{B}$. However, the very notion of the magnetic field $\boldsymbol{B} = \boldsymbol{\nabla} \times \boldsymbol{A}$ loses its physical meaning in a phase with the restored electroweak symmetry, which is suggested to be induced by this same field. Indeed, the definition of the electromagnetic gauge field $A^\mu = (A^0, \boldsymbol{A})$ (and, therefore, of $\boldsymbol{B}$) depends on the direction of the condensate of the Higgs doublet field $\langle\phi\rangle$ in the internal SU(2) space. For example, in the broken phase, the electromagnetic field (7) is identified in the unitary gauge where the upper component of $\langle\phi\rangle$ vanishes while the lower component is kept nonzero. As we expect that the magnetic field can restore the electroweak symmetry, $\langle\phi\rangle \to 0$, the electromagnetic direction becomes an ill-defined quantity, thus questioning the very meaning of the magnetic field $\boldsymbol{B}$ itself.

The flux quantization of an Abelian flux (14) is the result of periodic boundary conditions imposed on the appropriate Abelian gauge field: the Wilson loop, which includes the whole cross-section of a periodically compactified space, equals a unity because the contributions from the opposite parallel segments of the loop cancel

each other exactly.

The loop is a product of the link transporters, which can be read off from the interaction of the gauge field with a matter field. In our case (13), the link transporter is the phase $e^{i\theta_{x,\mu}}$, where, as we mentioned above, $\theta_{x,\mu} = a(g'/2)Y_\mu(x)$ in a continuum limit. The total flux (14) in a periodic space can therefore introduce the hypermagnetic fluxes only in pairs (namely, $2k$ vortices for $k \in \mathbb{N}$) due to the presence of the $g'/2$ factor in the interaction term (6). A similar situation also appears in QCD, where the fractional electric charge of quarks, $+2e/3$ and $-2/3$, leads to the quantization of the magnetic fluxes in triples [65].

Thus, the flux quantization of the hypermagnetic flux (and, therefore, the value of a possible minimal nonzero flux) is a result of the periodic boundary conditions rather than a consequence of the lattice discretization. The latter introduces an ultraviolet cutoff which sets an upper bound, $k_{\max} = L^2/2$, on the total number k of *pairs* of the elementary hypermagnetic fluxes that can be introduced on the lattice: $k = 0, 1, \ldots, L^2/2$.

We introduce the hypermagnetic field (14) as a hypercharge field $\theta^Y_{\mathrm{x},\mu}$ similarly to the standard practices [65]:

$$\theta^Y_{x,2}(k) = \frac{2\pi k}{L_s^2} x\,, \qquad \theta^Y_{x,1}(k)|_{x=L_s-1} = -\frac{2\pi k}{L_s} y\,, \quad (15)$$

with $\theta^Y_{x,3} = \theta^Y_{x,4} = 0$. Alternatively, one could introduce the hypermagnetic field via a "chemical potential" for the magnetic flux [37] that, as we checked, gives an identical result.

Notice that the emergence of possible mixed phases is not disfavored by the uniform nature of the hypermagnetic background field (14) since the background field fixes only the global flux through the whole lattice cross-section without affecting the local structures corresponding to possible inhomogeneities in the field.

Section C: Masses and physical point

We fix the ratio of the masses of the Higgs particle as well as the Z and W bosons to their physical values at a vanishing hypermagnetic field. To this end, we calculate the following slice-slice correlation functions:

$$C^H(l) = \frac{1}{L_t}\sum_{t=0}^{L_t-1} \left\langle \rho^2(t)\cdot\rho^2(t+l)\right\rangle\,, \quad (16)$$

$$C^Z_\mu(l) = \frac{1}{L_t}\sum_{t=0}^{L_t-1} \left\langle z_\mu(t)\cdot z_\mu(t+l)\right\rangle\,, \quad (17)$$

$$C^W_\mu(l) = \frac{1}{L_t}\sum_{t=0}^{L_t-1} \left\langle w^*_\mu(t)\cdot w_\mu(t+l)\right\rangle\,, \quad (18)$$

where the gauge-invariant quantities,

$$\rho^2(t) = \frac{1}{V_s}\sum_{x\in V_s} \left(\phi^\dagger_x\phi_x\right)(t)\,, \quad (19)$$

$$z_\mu(t) = \frac{1}{V_s}\sum_{x\in V_s} z_{x,\mu}(t)\,, \quad (20)$$

$$w_\mu(t) = \frac{1}{V_s}\sum_{x\in V_s} U^{12}_{x,\mu}(t)\,, \quad (21)$$

$$z_{x,\mu} = \arg\left(\phi^\dagger_x e^{i\left(\theta_{x,\mu}+\theta^Y_{x,\mu}\right)} U_{x,\mu}\phi_{x+\hat\mu}\right)\,, \quad (22)$$

are given by the spatial averaging over the spatial volume $V_s = L_s^3$ for each time slice fixed by the Euclidean time t.

We extract the physical Higgs mass m_H from the correlation function (16) of the ρ^2 field (19) following Ref. [49]. The definition of the lattice Z-boson field (20) in the correlator (17) comes from the form of the interaction term of the lattice action (13). It corresponds to the continuum neutral vector Z boson field (8) which is rigidly fixed by the covariant derivative (6) which appears in the continuum action (3). The two-point correlation function (18) includes the off-diagonal component $U^{12}_{x,\mu}$ of the $SU(2)$ matrix $U_{x,\mu}$ which corresponds to the physical W field in the Unitary gauge. In our calculations, we fix the Unitary gauge for the $SU(2)_W$ subgroup supplemented by the maximal tree gauge for the $U(1)_Y$ subgroup. The gauge fixing is needed to correctly identify the W-boson field and reduce the noise associated with the residual Abelian gauge freedom. To reduce the effect of the perturbative noise further, we use the spatial APE-smearing procedure [67] with parameters $\alpha_{\mathrm{APE}} = 0.5$ and $n_{\mathrm{APE}} = 100$ with respect to the $U_{x,\mu}$ and $\theta_{x,\mu}$ fields.

The numerical results for the two-point functions (16), (17) and (18) are then fitted by the exponential function,

$$C(l) = C_0\left(e^{-M\,l} + e^{-M\,(L_t-l)}\right) + C_1\,, \quad (23)$$

where the amplitude C_0, the (squared) condensate C_1, and the lattice mass M are the fit parameters. The lattice mass $M \equiv M^{\mathrm{lat}} = M^{\mathrm{phys}}a$ is related to the physical mass M^{phys} via the lattice spacing a. The examples of the fits (23) of all three correlators (16), (17) and (18) are provided in Fig. 4. Table I shows the masses and corresponding to the set of parameters used in the paper.

The correct choice of the ratios of the W, Z, and Higgs boson masses is essential for determining the correct structure of the vortex ground state [15, 18, 19].

The determination of the SU(2) gauge coupling seems to provide us with the uncertainty that has been, fortunately, resolved a few decades ago. In the literature, one customarily sets $\beta = 8$ for the SU(2) lattice coupling since this value corresponds to the renormalized $SU(2)$ gauge coupling $g^2_R \simeq 0.5$ which, in turn, lies closely to its phenomenological value in continuum limit [49, 50, 53]. We also explored other values of the SU(2) coupling constant. We ensured that all the conclusions of our paper

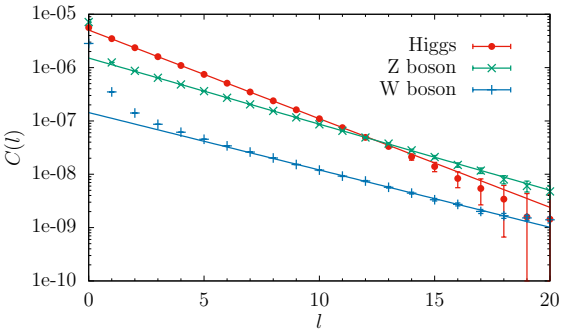

FIG. 4. The correlation functions for the Higgs (16), Z-boson (17), and W-boson (18) fields that are used for calculate the their masses at a vanishing background hypermagnetic field, $B_Y = 0$, via the fits by the function (23)

.

β	β_Y	λ	κ	$m_H a$	m_Z, GeV	m_W, GeV
12	10.45	0.175	0.4030	0.3827(9)	93.42(24)	81.1(6)

TABLE I. Parameters of the lattice Lagrangian (13), the corresponding lattice spacing a (expressed in terms of the Higgs mass $m_H = 125.25(17)\,\mathrm{GeV}$ [68]), and the masses of the W and Z bosons. Set 1 corresponds to the physical point (given to the Particle Data Group [68], $m_W = 80.377(12)\,\mathrm{GeV}$, $m_Z = 91.1876(21)\,\mathrm{GeV}$). The Weinberg angle θ_W equals to its physical value with the relative error of less than 2%.

are independent of the actual value of β in a wide set of values, provided the mentioned mass ratios are kept fixed. This property is valid even on the quantitative level, including the positions of the phase transitions. In our paper, we use $\beta = 12$ for which we have the best statistics. In the paper, we use the set of the lattice parameters shown in Table I.

The value of the lattice spacing for the physical point allows us to achieve the resolution of the hypermagnetic field about 10% in units of the first critical field B_{c1}. The finite resolution, which appears as a result of the quantization of magnetic flux, provides us with the systematic uncertainty in estimating the values of the critical magnetic fields (10) and (11).

In our simulations, we choose the lattice Higgs mass around the value $m_H a \simeq 0.38$ which corresponds to the lattice W-boson mass $m_W a \simeq 0.25$ at a vanishing background field $B_Y = 0$. For our lattice 64×48^3, this choice of the lattice spacing allows us to reach sufficient accuracy for all mass correlators while, at the same time, making it possible to achieve an acceptably small value of elementary hypermagnetic flux that determines the distance between nearest values of the hypermagnetic field (14). The latter factor is crucial for the precise determination of the magnetic-field-induced transitions with sufficient accuracy because of the elementary flux given the computational restrictions imposed on the maximal lattice volume.

The values of our quartic coupling λ and the parameter κ, shown in Table I, are different from typical values used in the literature to investigate the finite-temperature phase transition in the dimensionally unreduced, 3+1 dimensional model. For example, after an adaptation to our notations, the quartic coupling used in a finite-temperature study of Ref. [54] lies in the $\lambda \simeq 0.02$, which is an order of magnitude smaller than our value. This difference can partially be explained by the fact that we work with a heavier (in physical units) Higgs particle. In addition, we aim to decrease the gap $\delta B_Y = 4\pi/(g' L^2 a^2)$ between the nearest values of the hypermagnetic field strengths (14) in order to resolve better the evolution of the vacuum properties with increasing hypermagnetic field. To this end, we need to increase the physical size of the spatial lattice, which implies, in particular, augmenting the physical length of the lattice spacing. On the other hand, we cannot set a too large since it would lead to substantial ultraviolet artifacts. In the finite-temperature studies, one tends, on the contrary, to choose the lattice spacing as smaller as possible in order to increase temperature and to reach the symmetry-restored part of the wide electroweak crossover.

Our choice of the lattice spacing provides a compromise between these two purely technical constraints. Moreover, the slight deviation of the m_Z and m_W masses from their phenomenological values is already of the order of the systematic resolution of the hypermagnetic field in our work. Therefore, we conclude that the present accuracy is sufficient for our purposes related to determining the approximate values of the critical fields and the nature of the new, magnetic-field-induced phases in the model.

Section D: Lattice observables

The evolution of the expectation value of the Higgs field squared with the magnetic field, Fig. 1(a), as well as the local excess of the Higgs expectation value in the transverse (x, y) plane, Fig. 3(i), have been numerically calculated using the following gauge-invariant operator:

$$\phi^2(\boldsymbol{x}) = \frac{1}{N_t N_z} \sum_{t,z} \phi_x^\dagger \phi_x \,. \tag{24}$$

We denote $\boldsymbol{x} = (x, y)$ the coordinate in the longitudinal plane. The sum in the longitudinal (t, z) plane is applied to all observables to diminish statistical fluctuations and increase the noise-to-signal ratio. This averaging is applied to all numerically calculated quantities in Fig. 3. To visualize the local Higgs structure in Fig. 3(i), we took a square of the local value of the condensate (24).

The (squared) components of the W field, $W_\parallel^2$ and $W_\perp^2$, are plotted, as function of the background magnetic field, in Fig. 2. The spatial behavior of the same components,

$W_\parallel$ and $W_\perp$, is visualized in Figs. 3(e) and 3(g), respectively. We calculate the squared condensates with the help of the gauge-invariant operator,

$$W^2_\mu(\boldsymbol{x}) = \frac{1}{N_t N_z}\sum_{t,z} w_{x,\mu}\,, \tag{25}$$

$$w_{x,\mu} = \frac{1}{2}\big[(1-\frac{1}{2}\mathrm{Tr}\,\left(\hat{n}_x U_{x,\mu}\hat{n}_{x+\hat{\mu}}U^\dagger_{x,\mu})\right)\big]\,, \tag{26}$$

where we introduced the auxiliary matrix field:

$$\hat{n}_x = n^a_x\sigma^a \equiv \vec{n}\cdot\vec{\sigma} \tag{27}$$

$$n^a_x = -\frac{\phi^\dagger_x\sigma^a\phi_x}{\phi^\dagger_x\phi_x}. \tag{28}$$

The field (26) is invariant with respect to the $U(1)_Y$ hypergauge subgroup of the entire electroweak group. Under the subgroup of SU(2) gauge transformations, the fields transform as follows:

$$SU(2)_W: \quad \left\{\begin{array}{rcl} U_{x,\mu} & \to & \Omega_x U_{x,\mu}\Omega^\dagger_{x+\hat{\mu}}, \\ \phi_x & \to & \Omega_x\phi_x, \\ \hat{n}_x & \to & \Omega_x\hat{n}_x\Omega^\dagger_x, \end{array}\right. \tag{29}$$

implying that the field (26) is a gauge-invariant quantity.

The meaning of the construction (26) becomes clear in the Unitary gauge, $\phi_x = (0,\rho)^T$, where the adjoint vector $\hat{n}_x$ points out to the third direction, $\hat{n}_x = \sigma_3$. In this gauge, the off-diagonal components of the W boson field $W_\mu = W^a_\mu\sigma^a/2$ correspond to the standard charged W bosons: $W^\pm_\mu = (W^1_\mu \mp iW^2_\mu)/\sqrt{2}$. Representing the SU(2) gauge field $U_{x,\mu}$ as an exponent of the continuum W field, $U_{x,\mu} = \exp\{i\frac{1}{2}aW^a_\mu\sigma^a\}$, and expanding Eq. (26) in terms of the lattice spacing a, one gets the W condensate squared, $|W_\mu|^2 = W^+_{x,\mu}W^-_{x,\mu}$:

$$w_{x,\mu} = \frac{1}{2}a^2W^+_{x,\mu}W^-_{x,\mu} + O(a^4)\,. \tag{30}$$

Here, no sum over the repeating index μ is implemented. Thus, in the continuum limit, the composite field (26) is proportional to the W condensate (squared) (30). While the unitary gauge has been assumed in the derivation of Eq. (30), the expression (26) is a gauge-invariant quantity implying that the association (30) of $w_{x,\mu}$ with the $|W_\mu|^2$ condensate works in any gauge.

In Fig. 2, we give the W condensate in the leading order in the lattice spacing a:

$$W^2_\perp \equiv \frac{1}{a^2}\left(w_{x,1}+w_{x,2}\right)\,. \tag{31}$$

The Z flux in Fig. 1(f) is defined, similarly to the W condensate, as a gauge-invariant expression:

$$Z_{12}(\boldsymbol{x}) = \frac{1}{N_t N_z}\sum_{t,z} Z_{x,12}\,, \tag{32}$$

$$Z_{x,\mu\nu} = \varphi_{x,\mu} + \varphi_{x+\hat{\mu},\nu} - \varphi_{x+\hat{\nu},\mu} - \varphi_{x,\nu}\,, \tag{33}$$

$$\varphi_{x,\mu} = \arg\left(e^{i(\theta_{x,\mu}+\theta^Y_{x,\mu})}\phi^\dagger_x U_{x,\mu}\phi_{x+\hat{\mu}}\right)\,. \tag{34}$$

In the continuum limit, Eq. (34) reduces, up to a factor, to the usual expression of the Z flux expressed via the Z boson field (8): $Z_{12} = \partial_1 Z_2 - \partial_2 Z_1$.

The fields $Z_\parallel$ and $Z_\perp$ in Fig. 1(h) and (l), respectively, are the longitudinal and the transverse components of the Z field defined via the lattice angle φ, Eq. (34):

$$Z_\mu(\boldsymbol{x}) = \frac{1}{N_t N_z}\sum_{t,z}\varphi_{x,\mu}\,. \tag{35}$$

The excess of the electromagnetic field,

$$\Delta B(\boldsymbol{x}) = \frac{1}{N_t N_z}\sum_{t,z}\bar{\theta}^{\,\mathrm{e.m.}}_{x,12}\,, \tag{36}$$

shown in Fig. 3(k), is expressed via the electromagnetic gauge-invariant flux:

$$\bar{\theta}^{\,\mathrm{e.m.}}_{x,\mu\nu} = \arg\Big(e^{i\theta_{x,\mu\nu}}\mathrm{Tr}\left[\frac{1}{2}(\mathbb{1}+n_x)V_{x,\mu\nu}\right]\Big)\,, \tag{37}$$

$$\theta_{x,\mu\nu} = \theta_{x,\mu} + \theta_{x+\hat{\mu},\nu} - \theta_{x+\hat{\nu},\mu} - \theta_{x,\nu}\,, \tag{38}$$

$$V_{x,\mu\nu} = V_{x,\mu}V_{x+\hat{\mu},\nu}V^\dagger_{x+\hat{\nu},\mu}V^\dagger_{x,\nu}\,, \tag{39}$$

$$V_{x,\mu} = \frac{1}{2}\big(U_{x,\mu} + n_x U_{x,\mu} n_{x+\hat{\mu}}\big)\,. \tag{40}$$

In the unitary gauge, the flux (37) is reduced to the standard expression of the magnetic field in terms of the photon gauge field (7). Being a gauge-invariant expression, Eq. (37) gives us the magnetic flux without a need for the gauge fixing.

Finally, the current $\boldsymbol{J}^Z_\perp$ in Fig. 3(m) is identified as a weak current coupled to the hypercharge field:

$$J^{(\theta)}_\mu(\boldsymbol{x}) = \frac{-2}{N_t N_z}\sum_{t,z}\mathrm{Im}\left(e^{i(\theta_{x,\mu}+\theta^Y_{x,\mu})}\phi^\dagger_x U_{x,\mu}\phi_{x+\hat{\mu}}\right)\,. \tag{41}$$

This neutral current corresponds to the variation of the matter action in the lattice electroweak Lagrangian (13) with respect to the lattice hypergauge vector field θ.